

Stratified NH and ND emission in the prestellar core 16293E in L1689N

A. Bacmann^{1,2}, F. Daniel^{1,2}, P. Caselli³, C. Ceccarelli^{1,2}, D. Lis^{4,5}, C. Vastel^{6,7}, F. Dumouchel⁸, F. Lique⁸, and E. Caux^{6,7}

¹ Univ. Grenoble Alpes, IPAG, F-38000 Grenoble, France

² CNRS, IPAG, F-38000 Grenoble, France

³ Max Planck Institute for Extraterrestrial Physics, Giessenbachstrasse 1, D-85748 Garching, Germany

⁴ LERMA, Observatoire de Paris, PSL Research University, CNRS, Sorbonne Universités, UPMC Univ. Paris 06, 75014 Paris, France

⁵ California Institute of Technology, Cahill Center for Astronomy and Astrophysics 301-17, Pasadena, CA 91125, USA

⁶ Université de Toulouse; UPS-OMP; Institut de Recherche en Astrophysique et Planétologie (IRAP), Toulouse, France

⁷ CNRS, IRAP, 9 Av. colonel Roche, BP 44346, 31028 Toulouse Cedex 4, France

⁸ LOMC-UMR 6294, CNRS-Université du Havre, 25 rue Philippe Lebon, BP 1123 – 76063 Le Havre Cedex, France

Received; accepted

ABSTRACT

Context. High degrees of deuterium fractionation are commonly found in cold pre-stellar cores and in the envelopes around young protostars. As it brings strong constraints to chemical models, deuterium chemistry is often used to infer core history or molecule formation pathways. Whereas a large number of observations is available regarding interstellar deuterated stable molecules, relatively little is known about the deuteration of hydride radicals, as their fundamental rotational transitions are at high frequencies where the atmosphere is mostly opaque.

Aims. Nitrogen hydride radicals are important species in nitrogen chemistry, as they are thought to be related to ammonia formation. Observations have shown that ammonia is strongly deuterated, with $[\text{NH}_2\text{D}]/[\text{NH}_3] \sim 10\%$. Models predict similarly high $[\text{ND}]/[\text{NH}]$ ratios, but so far only one observational determination of this ratio is available, towards the envelope of the protostar IRAS16293-2422. In order to test model predictions, we aim here at determining $[\text{ND}]/[\text{NH}]$ in a dense, starless core.

Methods. We observed NH and ND in 16293E with the HIFI spectrometer on board the *Herschel* Space Observatory as part of the CHESST guaranteed time key programme, and derived the abundances of these two species using a non-LTE non-local radiative transfer model.

Results. Both NH and ND are detected in the source, with ND in emission and NH in absorption against the continuum arising from the cold dust emission. Our model shows however that the ND emission and the NH absorption originate from different layers in the cloud, as further evidenced by their different velocities. In the central region of the core, we can set a lower limit to the $[\text{ND}]/[\text{NH}]$ ratio of $\geq 2\%$. This estimate is consistent with recent pure gas-phase models of nitrogen chemistry.

Key words. Astrochemistry — Radiative transfer — ISM: molecules — ISM: abundances

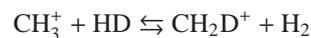
1. Introduction

Cold and dense regions of the interstellar medium like protostellar envelopes or prestellar cores have long been known to display high degrees of molecular deuterium fractionation (e.g. Jefferts et al. 1973). Despite a low elemental interstellar D/H ratio of $\sim 1.5 \cdot 10^{-5}$ (Linsky et al. 2006), the abundance ratios of deuterated molecules over their hydrogenated counterparts can reach from a few percent up to several tens of percent, depending on the species and the source. Doubly and triply deuterated species like CD_3OH or ND_3 have been detected in cold and dense gas, with fractionation ratios as high as 0.1% for $[\text{ND}_3]/[\text{NH}_3]$ (Lis et al. 2002b) and 1% for $[\text{CD}_3\text{OH}]/[\text{CH}_3\text{OH}]$ (Parise et al. 2004) the latter representing an enrichment of over 11 orders of magnitude over the $[\text{HD}]/[\text{H}_2]$ ratio. This abundance enhancement in deuterated molecules has its origins in the difference of zero-point energies between H_3^+ and its deuterated isotopologue H_2D^+ , so that the exchange reaction:



is slightly exothermic, and favours the formation of H_2D^+ (Watson 1976). The exothermicity of this reaction will depend

on the spin-state of the molecular species (Pagani et al. 1992; Flower et al. 2006; Pagani et al. 2011). As H_2 is mainly in its *para* form in dark clouds (Pagani et al. 2009), the reverse reaction does not proceed at low temperature and the formation of H_2D^+ is favoured. Finally, it is only when abundant species that are H_3^+ destroyers, like CO, start freezing out onto the grains that reaction (1) becomes the major destruction route for H_3^+ , increasing the abundance ratio $[\text{H}_2\text{D}^+]/[\text{H}_3^+]$. H_2D^+ can then transfer its deuteron to other species via ion-molecule reactions such as: $\text{CO} + \text{H}_2\text{D}^+ \rightarrow \text{DCO}^+ + \text{H}_2$ (Dalgarno & Lepp 1984). Reactions similar to (1) involving multiply deuterated isotopologues of H_3^+ also contribute to the increase in the molecular D/H ratio (Phillips & Vastel 2003; Roberts et al. 2003; Walmsley et al. 2004). Analogous mechanisms are thought to be at work with the reactions



so that CH_2D^+ and C_2HD^+ may contribute to deuteration (Parise et al. 2009). These reactions are more exothermic than

reaction (1) and are therefore believed to be dominant in warmer environments where reaction (1) is no longer efficient (see Roueff et al. 2013, for a comprehensive discussion on CH_2D^+).

As it depends sensitively on molecular depletion, deuteration can be used to probe the history of molecular cloud formation (Caselli & Ceccarelli 2012; Pagani et al. 2013; Ceccarelli et al. 2014; Brünken et al. 2014). Indeed, the molecular D/H is expected to increase with time, as the core condenses and its density increases, and CO depletion sets in.

Deuterium fractionation in ammonia has been observed to be very high (Roueff et al. 2000). These fractionation ratios were well accounted for by pure gas-phase models (Roueff et al. 2005). The model of Roueff et al. (2005) also predicts high D/H ratio in nitrogen hydride radicals (e.g. NH, NH_2), which are important by-products of ammonia formation. These species are believed to be formed at late stages, because they originate from molecular nitrogen N_2 , which in turn is the product of (much slower) neutral-neutral chemistry (Le Gal et al. 2014).

Observationally, nitrogen hydride radicals have long been elusive in dark cloud cores: because of their low moments of inertia, these species have their fundamental rotational transitions in the submillimeter to far-infrared range, where the high atmospheric opacity makes ground-based observations at best extremely challenging. The *Herschel* Space Observatory with the heterodyne spectrometer HIFI has enabled the observations of hydrides in the 500 GHz–2 THz range at an unprecedented sensitivity and spectral resolution. Nitrogen hydride radicals NH and NH_2 have been detected in the envelope of the Class 0 protostar IRAS 16293-2422, where they are seen in absorption against the continuum produced by the warm dust close to the central protostellar source (Hily-Blant et al. 2010). Deuterated imidogen, ND, was also detected by Bacmann et al. (2010) in the same source, and the derived $[\text{ND}]/[\text{NH}]$ ratio was found very high (around 70%).

Deuterated molecules are also used to probe chemical pathways. In the case of nitrogen hydrides, NH is believed to form mostly from the dissociative recombination of N_2H^+ (Roueff et al. 2015; Dislaire et al. 2012; Hily-Blant et al. 2010), whereas NH_2 is a product of the dissociative recombination of hydride ions like NH_3^+ and NH_4^+ , themselves coming from successive hydrogenations of N^+ by H_2 . Deuterium fractionation should reflect the different formation paths, as it is expected to be different depending on the origin of the deuteration. Indeed Roueff et al. (2005) find the $[\text{ND}]/[\text{NH}]$ ratio larger by a factor of 10 than the $[\text{NHD}]/[\text{NH}_2]$ ratio.

Many studies of deuterium fractionation are based on the ratio integrated along the line of sight, and make therefore the implicit assumption that the considered molecule and its deuterated counterpart are coexistent. However, conditions required to form the hydrogenated species may be different from those necessary to produce high deuterium fractionations, so that the deuterated species may not coexist everywhere with its hydrogenated counterpart (see e.g. Caselli et al. 2002). Here we present *Herschel*/HIFI observations of NH and ND in the 16293E prestellar core, a source which is in the vicinity of the Class 0 protostar IRAS 16293-2422. The source is known to harbour high abundances of deuterated molecules (Loinard et al. 2001; Lis et al. 2002a; Vastel et al. 2004), and to have moderately cold temperatures for a starless core (around 15 K – Stark et al. 2004), making it easier to detect species in absorption against the dust continuum emission. The observations are described in Section 2 and a first order LTE analysis in Section 3. In Section 4 we present our non-LTE non-local radiative transfer modeling of the source and discuss the findings in Section 5. In

this paper, square brackets refer to abundances with respect to H_2 .

2. Observations

The source 16293E was observed with HIFI (de Graauw et al. 2010) on board the *Herschel* Space Observatory (Pilbratt et al. 2010) as part of the guaranteed time key programme CHES (Ceccarelli et al. 2010). The ND ($N_J = 0_1 - 1_2$) transition at 522 GHz was observed on August 26, 2011 (observation ID 1342227402) and the NH ($N_J = 0_1 - 1_2$) transition at 974 GHz on September 15, 2011 (observation ID 1342228623), with both the acousto-optic wide band spectrometer (WBS, spectral resolution 1.1 MHz, corresponding to a velocity resolution of 0.6 km/s at 522 GHz and 0.35 km/s at 974 GHz) and the high resolution spectrometer (HRS, spectral resolution 0.25 MHz, corresponding to 0.15 km/s at 522 GHz and 0.08 km/s at 974 GHz). The observing mode used was the dual beam switch with optimisation of the continuum. In this mode an internal mirror is moved to provide two symmetric OFF positions situated 3' on either side (east and west) of the ON position. For 16293E, one of the OFF positions is close to an outflow driven by the protostar IRAS 16293-2422, where we do not expect ND emission. We have checked the OFF positions and found they showed no detectable signal.

Integration times (ON+OFF) were 80 minutes on ND and nearly 8 hours on NH. The source coordinates for the integration were $\alpha_{2000} = 16^{\text{h}}32^{\text{m}}28.6^{\text{s}}$, $\delta_{2000} = -24^{\circ}29'03''$. This position corresponds to the peak of the DCO^+ emission mapped by Lis et al. (2002a). The *Herschel* full width at half maximum beam sizes were 41'' at 522 GHz and 22'' at 974 GHz (Roelfsema et al. 2012).

The heterodyne data were processed with the standard HIFI pipeline version 8 up to level 2 products, after which they were exported to Gildas/CLASS¹ data format. Further analysis consisted of averaging individual spectra in both horizontal and vertical polarisations for the two backends and fitting a straight line to line-free regions in order to remove a baseline. The line brightness was converted to the main beam temperature using the latest estimate² of the forward and beam efficiencies, i.e. $B_{\text{eff}} = 0.64$ at 522 GHz, $B_{\text{eff}} = 0.65$ at 974 GHz, and $F_{\text{eff}} = 0.96$. The rest of the heterodyne data analysis was performed in CLASS.

In the frequency ranges where hyperfine components of NH and ND are expected (and corresponding image bands, as our observations are double side-band), we have verified the absence of contamination from lines of other species. Each detected transition in the observed spectrum correspond to a component of the NH or ND transition. Moreover, spectroscopic catalogues (JPL and CDMS) contain very few transitions which would be detectable in the physical conditions prevailing in prestellar cores (i.e. typically with $A_{ij} > 10^{-7} \text{ s}^{-1}$ and $E_{\text{up}} < 50 \text{ K}$ for emission lines or $E_{\text{lo}} < 50 \text{ K}$ for absorption lines, and these frequencies do not correspond to any detected feature of the spectrum). The rest frequencies and relative intensities of the hyperfine components for the observed NH and ND transitions are listed in Appendix A.

In addition to the heterodyne data, we also used continuum data in order to take into account molecular excitation by the photons emitted by the dust. Maps of 16293E at 160 μm taken from the PACS instrument (Poglitsch et al.

¹ <http://www.iram.fr/IRAMFR/GILDAS>

² http://herschel.esac.esa.int/twiki/pub/Public/HifiCalibrationWeb/HifiBeamReleaseNote_Sep2014.pdf

2010) aboard *Herschel* and at 250, 350, and 500 μm from the SPIRE instrument (Griffin et al. 2010) were taken as part of the *Herschel* Gould Belt survey guaranteed time key program (André et al. 2010). The PACS data (observation ID 1342241499 and 13422414500) consisted of two maps scanned in orthogonal directions in order to suppress the $1/f$ noise of the detectors. The data were processed within the HIPE (version 12.0) environment with the Scanamorphos reduction and map reconstruction algorithm (Roussel 2013). In addition, we subtracted from the whole image a constant offset determined from an apparently emission-free area to the South-East of the L1689 cloud. This works as a first order approximation to remove the emission of the telescope. For the SPIRE observations (observation ID 1342205093 and 1342205094), we used the level 2.5 maps automatically processed by the pipeline and calibrated for extended sources. Absolute calibration using HFI data from the *Planck* Satellite are also performed by the pipeline. The angular resolutions of the continuum maps are 18, 25, and 36'' for the SPIRE maps at 250, 350, and 500 μm (for more details, see Kirk et al. 2013), respectively, and around 14'' for the PACS map. Ground based observations at 850 μm from the James Clerk Maxwell 15 m Telescope (JCMT) on Mauna Kea were taken with the SCUBA-2 bolometer array (Holland et al. 2013) as part of the JCMT Gould Belt Survey. The data are presented in Pattle et al. (2015) where the data reduction procedure is also described. The 1.3 mm continuum map was taken at the IRAM 30 m telescope on Pico Veleta, Spain with the MPIfR bolometer array and is published in Lis et al. (2002a). The beams were 14.1'' for the JCMT map and 11'' for the IRAM 30 m map.

The distance to the source is taken to be 120 pc (Knude & Hog 1998; Loinard et al. 2008).

3. Results

The ND transition (lower panel in Fig. 1) is detected in emission above a continuum of about 0.067 K (single side band value) and the hyperfine components are mostly resolved. The *rms* on the spectrum in 1 MHz channels is less than 3 mK. The NH transition at 974.5 GHz (upper panel in Fig. 1) is detected in absorption, and its hyperfine components are also mostly resolved. The continuum level however oscillates by several tens of mK over each 1 GHz spectral window of the WBS and can therefore not be relied on. However, fitting a greybody curve to the continuum taken in the same source at other frequencies with HIFI yields estimates of the continuum around 0.07 K (see Appendix B).

In a first order analysis, we fitted the hyperfine components of the ND and NH transitions using the HFS method in CLASS, the same way as described in Bacmann et al. (2010). The HFS fit yields the source velocity, the line width, the excitation temperature as well as the line opacities. We fitted both the WBS spectra which have better signal-to-noise but lack spectral resolution as well as the HRS spectra in order to have a better estimate of the line width. The source velocities given by the fits are 3.53 ± 0.02 km/s for ND and 4.0 ± 0.01 km/s for NH, indicating that the NH producing the absorption and the ND producing the emission may not be spatially coexistent. This is reminiscent of the velocity differences seen in this source, where the velocity of the emission from deuterium bearing species like DCO^+ , N_2D^+ (Lis et al. 2002a), H_2D^+ and D_2H^+ (Vastel et al. 2004, 2012) or ND_2H (Gerin et al. 2006), as well as from dense gas tracers like N_2H^+ (Castets et al. 2001) are close to 3.5 – 3.7 km/s whereas those of lower-density tracers (e.g. H^{13}CO^+ , C^{18}O and C^{17}O - Lis et al. 2002a; Stark et al. 2004) are at the cloud velocity of 3.8 – 4 km/s. The line widths found by fitting the HRS spec-

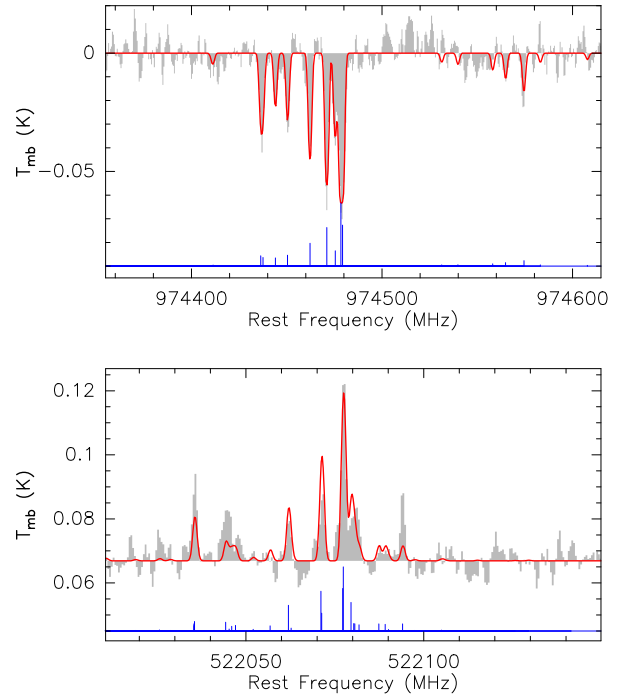


Fig. 1: Observed spectra of NH (top) and ND (bottom) in grey histograms, with the LTE model as a red solid line. As the continuum is unreliable for NH, it has been subtracted from the spectrum. The LTE fit poorly reproduces the relative line ratios in ND. A schematic view of the hyperfine structure indicating the frequencies and relative intensities of the hyperfine components is shown at the bottom of each spectrum (blue).

tra are 0.4 ± 0.02 km/s for both ND and NH, consistent with line widths measured in this source in other hydrides like ND_2H (Lis et al. 2006). Finally, we refer the reader to the discussion in Vastel et al. (2012) where more details on these various points can be found. For ND, the hyperfine components ratios are poorly reproduced in the LTE approach, as illustrated in Fig. 1. This indicates non-LTE effects (including, for example, excitation effects due to component overlap) which can arise in the case of high opacities. The opacities found by the fit in the case of ND are likely underestimated, as they are found quite low (~ 1.7 for the total opacity summed over all hyperfine components). The column densities for ND and NH using the LTE approximation are $1.1 \cdot 10^{13} \pm 0.9 \cdot 10^{13} \text{ cm}^{-2}$ and $5.8 \cdot 10^{13} \pm 1.3 \cdot 10^{13} \text{ cm}^{-2}$, respectively. The method used to derive these values is described in more details in Bacmann et al. (2010). The NH column density is found not to be sensitive to the value of the continuum intensity for continuum temperatures below 0.5 K. This is due to the large energy difference between the $J=0$ and $J=1$ levels so that the $J=1$ level is not populated and $h\nu \gg kT_{\text{ex}}$. The excitation temperature for NH (as derived from the HFS fit) is found to be around 5 K if we assume the continuum to be 0.07 K, and the total opacity (summed over all hyperfine components) is 12.5.

4. Radiative transfer modelling

Because of the poor fit of the hyperfine component ratios in ND and the velocity difference between ND and NH, we decided to take advantage of the new NH and ND collisional data recently published (Dumouchel et al. 2012) and used a more com-

prehensive non-LTE radiative transfer model in order to reproduce both spectral and continuum observations. The radiative transfer model takes into account line overlap for excitation as well as possible radiative excitation by dust. A detailed description of the code can be found in Daniel & Cernicharo (2008).

4.1. Continuum

We first built a model of the physical structure of the 16293E core, based on continuum observations at 160, 250, 350, 500, 850 μm and 1.3 mm (see Sect. 2).

A first step of the analysis consisted in performing a radial average of the continuum maps. Since the IRAS 16293-2422 protostar is located at the North-West from the core, at $\alpha = 16^{\text{h}}32^{\text{m}}22.73^{\text{s}}$, $\delta = -24^{\circ}28'32.2''$ (J2000), we removed from the average all the points located less than $80''$ from this position. The center of the radial profile is taken at the mean of the maxima at 850 μm and 1.3mm, i.e. R.A. = $16^{\text{h}}32^{\text{m}}28.8^{\text{s}}$, Dec. = $-24^{\circ}29'4''$ (J2000), which is offset by $\sim 3''$ with respect to the position where NH and ND were observed, well within the beams of the heterodyne observations. The radial averages of the continuum maps are reported in Fig. 2.

Since the computation of the radiative transfer is time-consuming, it was not possible to explore the complete parameter space. We therefore tried several types of density profiles before adopting a piecewise powerlaw profile, as in Daniel et al. (2013), with a constant density value from $r = 0$ to $r = r_0$ and a power-law index of α beyond r_0 and up to r_{out} . We fixed the innermost limiting radius at $r_0 = 4''$, as in Stark et al. (2004), and the external radius at $r_{\text{out}} = 350''$. Moreover, we assumed a value of $\kappa_{1300} = 0.005 \text{ cm}^2 \text{ g}^{-1}$ for the dust absorption coefficient at 1.3 mm (Ossenkopf & Henning 1994). This density structure can well account for the continuum emission profiles while keeping the number of free parameters at a minimum. The only free parameters of the model are the central density n_0 , the slope α , the dust emissivity spectral index β , and the dust temperature radial profile. In order to further reduce the number of models, we opted to fix the dust temperature profile and then run a grid of models with free parameters n_0 , α and β . We started with the most simple assumption of a uniform temperature across the core. Doing so, the most acceptable model is obtained for $T_d \sim 14 \text{ K}$. For this dust temperature, the model parameters are in the range $1.3 < \alpha < 1.7$, $1.2 < \beta < 1.8$ and $5 \cdot 10^6 < n_0 < 2 \cdot 10^7 \text{ cm}^{-3}$. However, with a uniform dust temperature, we could not find a model that would fit satisfactorily the radial intensities at every wavelengths. Moreover, the dust exponent of the best models are found around $\beta \sim 1.5$, which is low by comparison to the exponent expected for the dust in low mass star forming regions. At this stage, we found that the usual correlation between the dust temperature and the β exponent is present, i.e. adopting a lower dust temperature lead to an increase in the value derived for β . However, the quality of the models is degraded by adopting a lower temperature while keeping the dust temperature uniform. Hence, we made the choice to set the dust opacity exponent to $\beta = 1.7$ (consistent with the value of 1.6 derived from Planck data - Planck Collaboration et al. 2014) and then investigated various dust temperature profiles that would enable to reproduce the observations. As in Stark et al. (2004), the dust temperature was assumed to increase outwards and we found a good solution by adopting a dust temperature that would vary from 11 K in the core centre up to 16 K in the outer envelope. These values are consistent with the temperature obtained from NH_3 observations by Wootten & Loren (1987). With such a gradient, the best models are obtained around $\alpha \sim 1.7$, $n_0 \sim 1.4 \cdot 10^7 \text{ cm}^{-3}$.

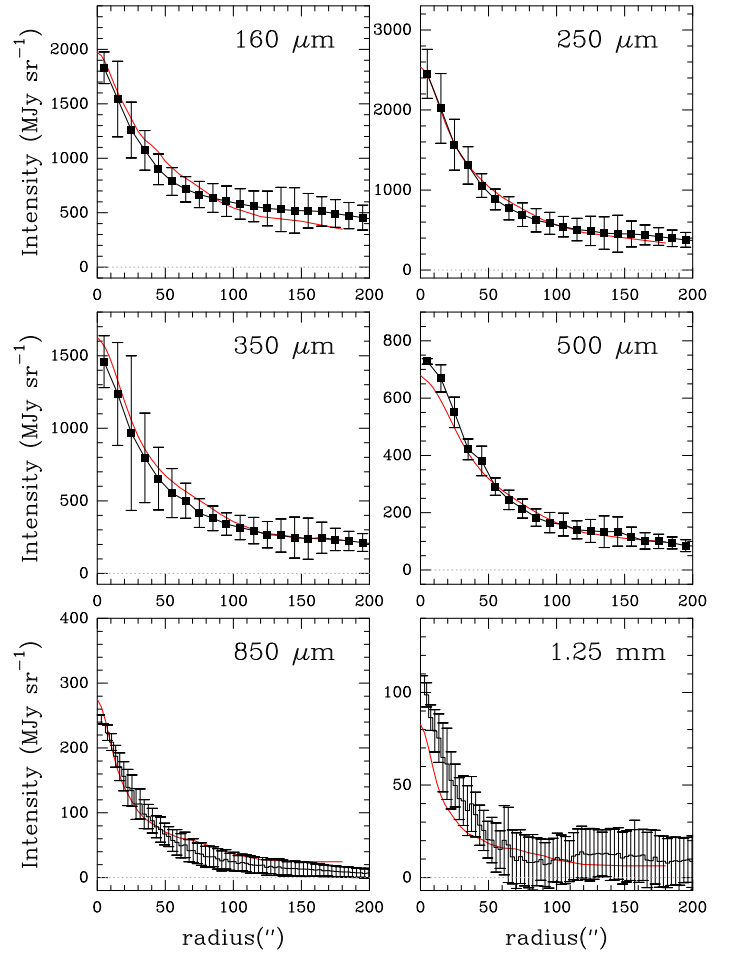


Fig. 2: Observed continuum surface brightness radial profiles from 160 μm to 1.3 mm (black curve). The model is overplotted in red.

The continuum radial profiles obtained with these parameters are compared to the observations in Fig. 2, and the associated physical structure, i.e. H_2 density and dust temperature profiles, is reported in Fig. 3. In Fig. 2, the error bars associated with the observations correspond to the spread of the observational points introduced by the radial average. As commented in Appendix B, we expect additional uncertainties in the absolute flux of the observations due to the calibration of the data, ranging from $\sim 15\%$ for the PACS data to $\sim 30\%$ for the ground based one. Hence, these uncertainties can account for the discrepancies between models and observations.

4.2. Molecules

The radiative transfer for the molecular line emission was solved using the 1Dart code (Daniel & Cernicharo 2008), which takes into account the hyperfine structure in the excitation calculations. We used the collisional rate coefficients of NH and ND with He from Dumouchel et al. (2012), which were scaled to account for the difference in reduced mass with H_2 . Spectroscopic data (frequencies, Einstein spontaneous emission coefficients, level energies, degeneracies) were originally determined by Saito & Goto (1993) and Klaus et al. (1997) for ND and NH,

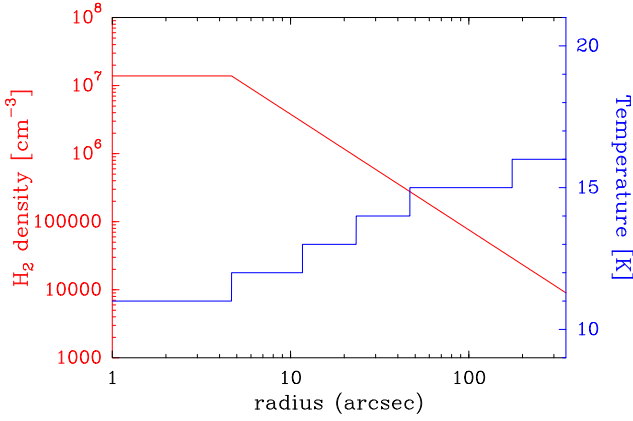


Fig. 3: H_2 density and dust temperature profiles derived from the continuum modeling.

respectively, and were obtained from the CDMS³ (Müller et al. 2001, 2005) database. In the case of ND, we found that considering line overlap effects influences the emergent intensities by a factor of ~ 2 .

In order to model the ND spectrum, we first tried to use a constant abundance throughout the envelope. However, under such an assumption, the resulting fits are rather poor since the abundance needed to produce enough emission in the lines of lowest opacity leads to self-absorption features in the most opaque lines which are by far too pronounced by comparison to the observations. Hence, we introduced two regions in the radial abundance profile (see Fig. 4). Given that NH and ND were observed toward a single position, we do not have enough observational constraints to derive precisely the respective sizes of these two regions. Indeed, from the modelling, we found that all the models with a central region of radius lower than $60''$ would give equivalent fits. Increasing this radius beyond $60''$ would lead to self-absorbed profiles in ND, which is not observed. However, the choice of the actual size of the innermost region affects the derived value of the ND abundance, and we estimate the uncertainty to be of a factor ~ 2 . In what follows, we arbitrarily set to $15''$ the size of the central region. We found a good solution setting the abundance to $[\text{ND}] = 1.6 \cdot 10^{-9}$ in this region and derived an upper limit of $[\text{ND}] = 1.5 \cdot 10^{-10}$ outside this radius (Fig. 5). With the radius of the central region set to $30''$, the central ND abundance would be $[\text{ND}] = 1.1 \cdot 10^{-9}$ instead.

For the NH modelling, we first tried a similar abundance profile to ND, scaled by a constant factor. However, by doing so, we could not reproduce the observations. In fact, we found that the region of the envelope where the abundance has to be increased in order to fit the observations corresponds to the region $r > 15''$. A reasonable fit to the observations is obtained by setting the NH abundance to $[\text{NH}] = 3 \cdot 10^{-9}$ in this region. Below $15''$, we arbitrarily kept the abundance of the outer region, i.e. $[\text{NH}] = 3 \cdot 10^{-9}$, since the models are not sensitive to this latter value. Indeed, even in the central region, the densities are not high enough to excite NH, so that the NH emission remains within the noise of the observations even for NH abundances of $\sim 4 \cdot 10^{-8}$.

The comparison between the modelled spectra and the observations is reported in Fig. 5, where the red spectrum represents our best fit. Other acceptable fits are shown as a grey area. They were determined by varying the ND and NH abundances in the inner and outer layers while keeping the physical structure (den-

sity and temperature profiles) as in the best fit (Sect. 4.1). The abundances as well as their uncertainties are shown in Fig. 4.

Finally, we stress that the current model most probably represents a simplistic view of the actual geometry of the region. Indeed, it was previously observed that the dust emission peak and the deuterium peak are offset by $\sim 15''$. We cannot account for such an offset in a 1D model and a 3D modelling would thus be required. Obviously, to constrain such a model, it would be necessary to have maps of NH and ND, which are currently unavailable. Additionally, by examining Fig. 5 it is worth noting that the comparison between the model and observations shows some discrepancies, especially if one considers the ratio between the hyperfine components. In fact, we found that by increasing the gas temperature, we could obtain a better fit to the observations. However, if we assume that the dust and gas are thermalized, we would have to decrease the dust opacity exponent below 1.7 in order to have a model still compatible with the continuum observations discussed in the previous section. Such a decrease would presumably be unlikely, as the dust emissivity spectral index tends to increase to values above 2 when the dust temperature decreases below 15 K (e.g. Paradis et al. 2011). In fact, it is important to keep in mind that the current model uses collisional rate coefficients scaled from the He rates. Such a procedure often leads to underestimate the actual rate coefficients with H_2 . As a consequence, if the rate coefficients are indeed underestimated, this could provide an alternate explanation for the discrepancies between the model and observations, and would not require to modify the gas temperature derived from the continuum. This subject will be addressed when the collisional rate coefficients with H_2 become available.

The column densities of ND and NH were determined by integrating the density multiplied by the abundance along the line of sight, and by convolving with a beam of the appropriate size. The values are $N(\text{ND}) = 6.0_{-2.3}^{+2.3} \cdot 10^{13} \text{ cm}^{-2}$ and $N(\text{NH}) = 6.4_{-3.1}^{+38.3} \cdot 10^{14} \text{ cm}^{-2}$. These values are a factor ~ 10 higher than the ones derived from the LTE analysis for NH, and a factor of ~ 6 higher for ND.

In summary, in order to obtain a reasonable fit of the NH and ND spectra, it is necessary to introduce two regions in the abundance radial profile. The ND emission originates primarily from the inner region and the NH absorption from the outer region. Consequently, the NH abundance in the inner region is poorly constrained and we can only set an upper limit to the ND abundance in the outer region. Adopting a non-LTE approach has allowed us to improve the fit of the ND spectrum, in particular the relative ratios of the hyperfine components are better reproduced than in the case of the LTE hypothesis.

5. Discussion

The current modelling of the NH and ND spectra observed towards 16293E requires to introduce a dichotomy between the two species. From the modelling, the ND emission originates in the innermost part of the core, while the NH absorption is mostly dominated by a region that surrounds it. Hence, the spectra of both species are found to be dominated by two regions which are spatially distinct. The separation between these two regions is further outlined considering the V_{LSR} associated with the lines. Indeed, the ND and NH spectra are consistent with V_{LSR} values that differ by $\sim 0.4 \text{ km s}^{-1}$. As a consequence, we conclude that discussing the $[\text{ND}]/[\text{NH}]$ abundance ratio is not meaningful, or at least largely uncertain, in the case of the 16293E prestellar core. At most, we can say that in the region where the ND abundance is constrained, the deuterium fractionation is larger than

³ <http://www.astro.uni-koeln.de/cdms/>

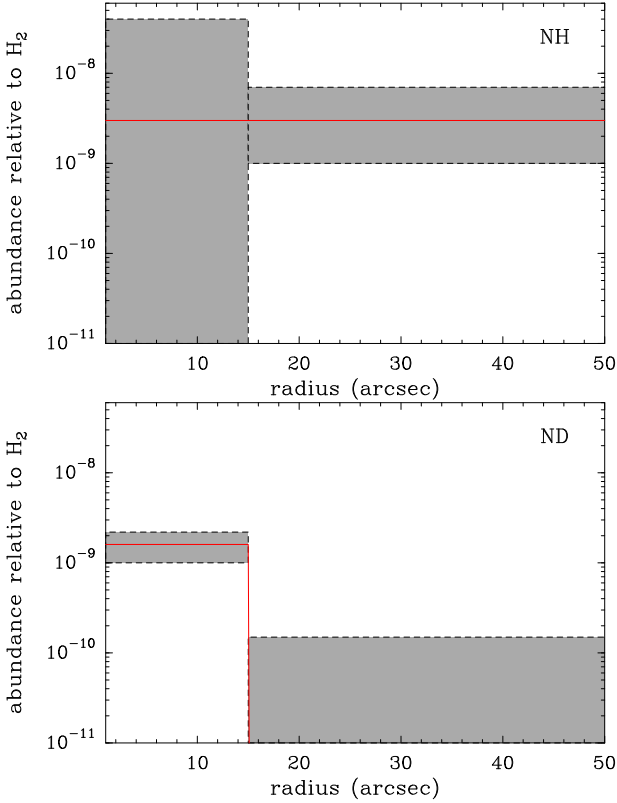


Fig. 4: NH and ND abundances as a function of radius. The grey area represents the uncertainty on the abundances (from the grey area in Fig. 5).

2%. In the outer region, an upper limit for $[\text{ND}]/[\text{NH}]$ is 20%. Recently, the formation chemistry of the NH isotopologues has been investigated by Hily-Blant et al. (2010) and Roueff et al. (2015). In both studies, the authors conclude that the main pathway leading to either NH or ND is through dissociative recombination of N_2H^+ or N_2D^+ with electrons. The upper and lower limits we infer for $[\text{ND}]/[\text{NH}]$, in the 16293E core, are consistent with the latest theoretical predictions of Roueff et al. (2015), since their model gives $[\text{ND}]/[\text{NH}] \sim 10\%$ at H_2 densities $\sim 10^5 \text{ cm}^{-3}$ and falls below 6% at $\sim 10^4 \text{ cm}^{-3}$.

By considering the current modelling, we note that the parameters we derived in order to describe the core, i.e. the H_2 density, the radial gas temperature profile or the parameters that describe the dust, may be subject to large uncertainties. This is a consequence of strong correlations between some model parameters, e.g. between the dust absorption coefficient and the central H_2 density n_0 , or between the dust temperature and the dust spectral index β . The uncertainty, which affects the individual parameters can be outlined by considering earlier estimates of, e.g., the central core density. As an example, from a model of dust emission maps at 450 and 850 μm , Stark et al. (2004) estimated the H_2 density to $1.6 \cdot 10^6 \text{ cm}^{-3}$ in the central 1000 AU, while our current estimate is a factor of 10 larger. Our estimate of the central density is however consistent with the qualitative conclusion reached by Lis et al. (2002b), from observation of a ND_2H line of high critical density. Indeed, Lis et al. (2002b) concluded that 16293E and L1544 should have comparable central densities, that would be typically a factor of two higher than the density in B1. Hence, though the central density value derived from the current modeling is high, it is consistent with the

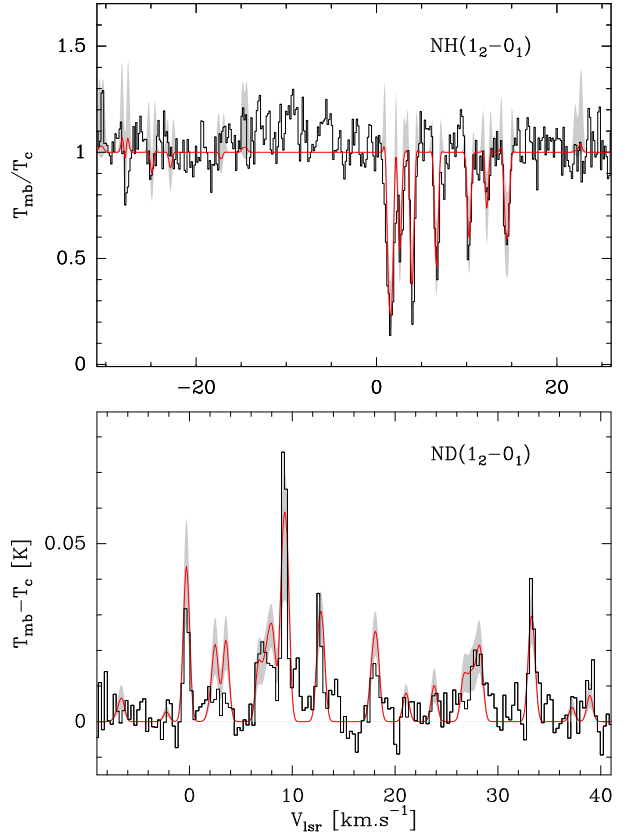


Fig. 5: Best-fit model (red line) of the non local, non-LTE radiative transfer analysis, superimposed on the observed spectrum (black line). The grey area represents the range of synthetic spectra consistent with the observations. The continuum level T_c has been subtracted from the ND spectrum. The NH spectrum is shown divided by the continuum level T_c .

latest estimate of the H_2 density in L1544 and B1, respectively estimated to $\sim 10^7$ within a central radius of 500 AU (Keto et al. 2014) and $3 \cdot 10^6 \text{ cm}^{-3}$ within a radius of 1175 AU (Daniel et al. 2013). Finally, given these uncertainties, we modelled the NH and ND spectra with alternate density and temperature profiles, where the central density was, at most, typically varied by a factor 3 according to the model discussed earlier. The temperature was varied by a few kelvins. The absolute abundances of NH and ND with respect to H_2 change accordingly (i.e. when the density is decreased by a given factor, the abundances increase by the same factor), but both the abundance profiles as well as the $[\text{ND}]/[\text{NH}]$ abundance ratios remain unchanged, so that the dichotomy between the NH and ND emission is still present in these models.

Prior to this work, ND was only detected once, in the direction of the IRAS 16293-2422 protostar (Bacmann et al. 2010). Its lines, along with the main isotopologue lines, were detected in absorption and it was deduced that both molecules would trace the cold envelope that surrounds the protostar. The abundance ratio between the two isotopologues was estimated to lie in the range $[\text{ND}]/[\text{NH}] \sim 30\text{-}100\%$. This range of values is larger than the upper limit of 20% we deduced for the extended component traced by NH, in direction of the 16293E prestellar core, but agrees with the lower limit we derived for the region where ND is detected. Finally, in the direction of the IRAS 16293-2422 protostar, it was found that some deuterated species, like HDO,

would trace an external foreground layer (Coutens et al. 2012; Wakelam et al. 2014), used to reproduce Herschel/HIFI CH observations (Bottinelli et al. 2014). In the current case, we cannot confirm nor discard the presence of this foreground layer in the direction of the 16293E core. Our data do not enable us to conclude about the origin of the velocity shift between the ND and NH spectra i.e. whether NH absorption arises in a foreground layer component, whether the denser gas is blueshifted because of its interaction with the outflow as suggested by Lis et al. (2002b), or whether the velocity difference could be due to gravitational contraction.

The fact that hydrogenated and deuterated species come from distinct physical regions, in L1689N, was previously recognized by Lis et al. (2002a). However, such a distinction would not necessarily be recognized for the molecules which are observed with insufficient velocity resolution. In the present case, because of the difference in excitation for the two species (the critical densities for the NH $1_2 - 0_1$ transitions are a factor of ten higher than those for the ND $1_2 - 0_1$ transition), NH does not emit in the central region where ND emission originates and the emission of hydrogenated and deuterated species are dominated by distinct physical regions. For a better determination of deuterium fractionation, lines with similar critical densities should be used for both the main species and its deuterated counterpart.

Acknowledgements. Nicolas Billot is acknowledged for his help in reducing PACS data in HIPE. We also thank Alexandre Faure for enlightening discussions about collisional excitation of hydrides. Support for this work was provided by NASA (*Herschel* OT funding) through an award issued by JPL/Caltech. P.C. acknowledges financial support of the European Research Council (ERC; project PALs 320620). This research has made use of data from the Herschel Gould Belt survey (HGBS) project (<http://gouldbelt-herschel.cea.fr>). The HGBS is a Herschel Key Programme jointly carried out by SPIRE Specialist Astronomy Group 3 (SAG 3), scientists of several institutes in the PACS Consortium (CEA Saclay, INAF-IFSI Rome and INAF-Arcetri, KU Leuven, MPIA Heidelberg), and scientists of the Herschel Science Center (HSC). This work has been supported by the Agence Nationale de la Recherche (ANR-HYDRIDES), contract ANR-12-BS05-0011-01.

References

- André, P., Men'shchikov, A., Bontemps, S., et al. 2010, *A&A*, 518, L102
 Aniano, G., Draine, B. T., Gordon, K. D., & Sandstrom, K. 2011, *PASP*, 123, 1218
 Bacmann, A., Caux, E., Hily-Blant, P., et al. 2010, *A&A*, 521, L42
 Bottinelli, S., Wakelam, V., Caux, E., et al. 2014, *MNRAS*, 441, 1964
 Brünken, S., Sipilä, O., Chambers, E. T., et al. 2014, *Nature*, 516, 219
 Caselli, P., Benson, P. J., Myers, P. C., & Tafalla, M. 2002, *ApJ*, 572, 238
 Caselli, P. & Ceccarelli, C. 2012, *A&ARv*, 20, 56
 Castets, A., Ceccarelli, C., Loinard, L., Caux, E., & Lefloch, B. 2001, *A&A*, 375, 40
 Ceccarelli, C., Bacmann, A., Boogert, A., et al. 2010, *A&A*, 521, L22
 Ceccarelli, C., Caselli, P., Bockelée-Morvan, D., et al. 2014, *Protostars and Planets VI*, 859
 Coutens, A., Vastel, C., Caux, E., et al. 2012, *A&A*, 539, A132
 Dalgarno, A. & Lepp, S. 1984, *ApJ*, 287, L47
 Daniel, F. & Cernicharo, J. 2008, *A&A*, 488, 1237
 Daniel, F., Gerin, M., Roueff, E., et al. 2013, *A&A*, 560, A3
 de Graauw, T., Helmich, F. P., Phillips, T. G., et al. 2010, *A&A*, 518, L6
 Dislaire, V., Hily-Blant, P., Faure, A., et al. 2012, *A&A*, 537, A20
 Dumouchel, F., Klos, J., Toboła, R., et al. 2012, *J. Chem. Phys.*, 137, 4306
 Flower, D. R., Pineau Des Forêts, G., & Walmsley, C. M. 2006, *A&A*, 449, 621
 Gerin, M., Lis, D. C., Philipp, S., et al. 2006, *A&A*, 454, L63
 Griffin, M. J., Abergel, A., Abreu, A., et al. 2010, *A&A*, 518, L3
 Griffin, M. J., North, C. E., Schulz, B., et al. 2013, *MNRAS*, 434, 992
 Hily-Blant, P., Maret, S., Bacmann, A., et al. 2010, *A&A*, 521, L52
 Holland, W. S., Bintley, D., Chapin, E. L., et al. 2013, *MNRAS*, 430, 2513
 Jefferts, K. B., Penzias, A. A., & Wilson, R. W. 1973, *ApJ*, 179, L57
 Kauffmann, J., Bertoldi, F., Bourke, T. L., Evans, N. J., & Lee, C. W. 2008, *A&A*, 487, 993
 Keto, E., Rawlings, J., & Caselli, P. 2014, *MNRAS*, 440, 2616
 Kirk, J. M., Ward-Thompson, D., Palmeirim, P., et al. 2013, *MNRAS*, 432, 1424
 Klaus, T., Takano, S., & Winnewisser, G. 1997, *A&A*, 322, L1
 Knude, J. & Hog, E. 1998, *A&A*, 338, 897
 Le Gal, R., Hily-Blant, P., Faure, A., et al. 2014, *A&A*, 562, A83
 Linsky, J. L., Draine, B. T., Moos, H. W., et al. 2006, *ApJ*, 647, 1106
 Lis, D. C., Gerin, M., Phillips, T. G., & Motte, F. 2002a, *ApJ*, 569, 322
 Lis, D. C., Gerin, M., Roueff, E., Vastel, C., & Phillips, T. G. 2006, *ApJ*, 636, 916
 Lis, D. C., Roueff, E., Gerin, M., et al. 2002b, *ApJ*, 571, L55
 Loinard, L., Castets, A., Ceccarelli, C., Caux, E., & Tielens, A. G. G. M. 2001, *ApJ*, 552, L163
 Loinard, L., Torres, R. M., Mioduszewski, A. J., & Rodriguez, L. F. 2008, *ApJ*, 675, L29
 Müller, H. S. P., Schlöder, F., Stutzki, J., & Winnewisser, G. 2005, *J. Mol. Struct.*, 742, 215
 Müller, H. S. P., Thorwirth, S., Roth, D. A., & Winnewisser, G. 2001, *A&A*, 370, L49
 Ossenkopf, V. & Henning, T. 1994, *A&A*, 291, 943
 Pagani, L., Lesaffre, P., Jorfi, M., et al. 2013, *A&A*, 551, A38
 Pagani, L., Roueff, E., & Lesaffre, P. 2011, *ApJL*, 739, L35
 Pagani, L., Salez, M., & Wannier, P. G. 1992, *A&A*, 258, 479
 Pagani, L., Vastel, C., Hugo, E., et al. 2009, *A&A*, 494, 623
 Paladini, R., Linz, H., Altieri, B., & Ali, B. 2012, *PACS/Herschel calibration report*, 1
 Paradis, D., Bernard, J.-P., Mény, C., & Gromov, V. 2011, *A&A*, 534, A118
 Parise, B., Castets, A., Herbst, E., et al. 2004, *A&A*, 416, 159
 Parise, B., Leurini, S., Schilke, P., et al. 2009, *A&A*, 508, 737
 Pattle, K., Ward-Thompson, D., Kirk, J. M., et al. 2015, *MNRAS*, 450, 1094
 Phillips, T. G. & Vastel, C. 2003, in *SFCHEM 2002: Chemistry as a Diagnostic of Star Formation*, ed. C. L. Curry & M. Fich, 3
 Pilbratt, G. L., Riedinger, J. R., Passvogel, T., et al. 2010, *A&A*, 518, L1
 Planck Collaboration, Abergel, A., Ade, P. A. R., et al. 2014, *A&A*, 571, A11
 Poglitsch, A., Waelkens, C., Geis, N., et al. 2010, *A&A*, 518, L2
 Roberts, H., Herbst, E., & Millar, T. J. 2003, *ApJ*, 591, L41
 Roelfsema, P. R., Helmich, F. P., Teyssier, D., et al. 2012, *A&A*, 537, A17
 Roueff, E., Gerin, M., Lis, D. C., et al. 2013, *J. Phys. Chem. A*, 117, 9959
 Roueff, E., Lis, D. C., van der Tak, F. F. S., Gerin, M., & Goldsmith, P. F. 2005, *A&A*, 438, 585
 Roueff, E., Loison, J.-C., & Hickson, K. M. 2015, *A&A*, 576, A99
 Roueff, E., Tiné, S., Coudert, L. H., et al. 2000, *A&A*, 354, L63
 Roussel, H. 2013, *PASP*, 125, 1126
 Saito, S. & Goto, M. 1993, *ApJ*, 410, L53
 Stark, R., Sandell, G., Beck, S. C., et al. 2004, *ApJ*, 608, 341
 Vastel, C., Caselli, P., Ceccarelli, C., et al. 2012, *A&A*, 547, A33
 Vastel, C., Phillips, T. G., & Yoshida, H. 2004, *ApJ*, 606, L127
 Wakelam, V., Vastel, C., Aikawa, Y., et al. 2014, *MNRAS*, 445, 2854
 Walmsley, C. M., Flower, D. R., & Pineau des Forêts, G. 2004, *A&A*, 418, 1035
 Watson, W. D. 1976, *Rev. Mod. Phys.*, 48, 513
 Wootten, A. & Loren, R. B. 1987, *ApJ*, 317, 220

Appendix A: Rest frequencies and relative intensities of observed NH and ND hyperfine components.

Table A.1 and A.2 list the rest frequencies of the observed hyperfine components in NH and ND. The relative intensities have been normalised so that their sum is equal to one. The data are adapted from the CDMS catalogue (Müller et al. 2001, 2005).

Appendix B: Spectral energy distribution of 16293E

From the continuum data described in section 2, we derived a spectral energy distribution for the position of integration in ND and NH (Fig. B.1). The continuum data were first smoothed to the spatial resolution of the coarsest map (Herschel/SPIRE at $500\ \mu\text{m}$), i.e. $36''$. To this effect, the PACS $160\ \mu\text{m}$, and SPIRE $250\ \mu\text{m}$, $350\ \mu\text{m}$ and $500\ \mu\text{m}$ were convolved with the appropriate kernels as described in Aniano et al. (2011). The SCUBA-2 map at $850\ \mu\text{m}$ and MPIfR bolometre map at $1.3\ \text{mm}$ were convolved using gaussian kernels of $\text{FWHM} = 33.2''$ and $\text{FWHM} = 34.3''$, respectively. The specific intensities given are those measured at the position of the ND integration. Error bars on the

Table A.1: NH frequencies and relative intensities of the hyperfine components of the 974.5 GHz transition.

Rest frequency (MHz)	Relative intensity
974315.58	$3.00 \cdot 10^{-5}$
974342.57	$1.70 \cdot 10^{-4}$
974354.64	$9.00 \cdot 10^{-5}$
974410.56	$1.71 \cdot 10^{-3}$
974411.39	$4.92 \cdot 10^{-3}$
974436.35	$4.38 \cdot 10^{-2}$
974437.54	$3.67 \cdot 10^{-2}$
974444.04	$3.47 \cdot 10^{-2}$
974450.44	$4.61 \cdot 10^{-2}$
974462.22	$9.68 \cdot 10^{-2}$
974471.00	$1.63 \cdot 10^{-1}$
974475.41	$6.48 \cdot 10^{-2}$
974478.38	$2.67 \cdot 10^{-1}$
974479.34	$1.73 \cdot 10^{-1}$
974531.32	$4.98 \cdot 10^{-3}$
974539.82	$6.20 \cdot 10^{-3}$
974558.07	$9.43 \cdot 10^{-3}$
974564.78	$1.47 \cdot 10^{-2}$
974574.43	$2.35 \cdot 10^{-2}$
974583.03	$4.97 \cdot 10^{-3}$
974607.78	$3.49 \cdot 10^{-3}$

Table A.2: ND frequencies and relative intensities of the hyperfine components of the 522.0 GHz transition.

Rest frequency (MHz)	Relative intensity
521982.65	$1.00 \cdot 10^{-5}$
521992.18	$2.20 \cdot 10^{-4}$
522001.05	$6.50 \cdot 10^{-4}$
522008.98	$1.57 \cdot 10^{-3}$
522010.65	$1.93 \cdot 10^{-3}$
522010.65	$1.60 \cdot 10^{-3}$
522018.95	$1.76 \cdot 10^{-3}$
522025.72	$3.19 \cdot 10^{-3}$
522028.73	$1.95 \cdot 10^{-3}$
522035.57	$2.23 \cdot 10^{-2}$
522035.57	$1.63 \cdot 10^{-2}$
522035.57	$2.96 \cdot 10^{-2}$
522044.32	$2.73 \cdot 10^{-2}$
522045.27	$6.01 \cdot 10^{-3}$
522046.00	$1.44 \cdot 10^{-2}$
522047.06	$1.76 \cdot 10^{-2}$
522052.07	$5.04 \cdot 10^{-3}$
522056.83	$1.61 \cdot 10^{-2}$
522061.94	$8.01 \cdot 10^{-2}$
522062.72	$8.95 \cdot 10^{-3}$
522071.29	$1.24 \cdot 10^{-1}$
522071.29	$5.57 \cdot 10^{-2}$
522077.37	$1.32 \cdot 10^{-1}$
522077.37	$2.00 \cdot 10^{-1}$
522079.53	$8.93 \cdot 10^{-2}$
522080.30	$2.31 \cdot 10^{-2}$
522080.64	$2.26 \cdot 10^{-2}$
522081.82	$1.93 \cdot 10^{-2}$
522087.35	$2.22 \cdot 10^{-2}$
522089.14	$2.05 \cdot 10^{-2}$
522090.05	$4.52 \cdot 10^{-3}$
522094.03	$2.22 \cdot 10^{-2}$
522097.43	$1.63 \cdot 10^{-3}$
522104.99	$2.66 \cdot 10^{-3}$
522105.87	$7.90 \cdot 10^{-4}$
522115.01	$8.10 \cdot 10^{-4}$
522125.61	$4.00 \cdot 10^{-4}$
522129.42	$8.70 \cdot 10^{-4}$
522141.23	$1.20 \cdot 10^{-4}$
522158.81	$1.00 \cdot 10^{-5}$

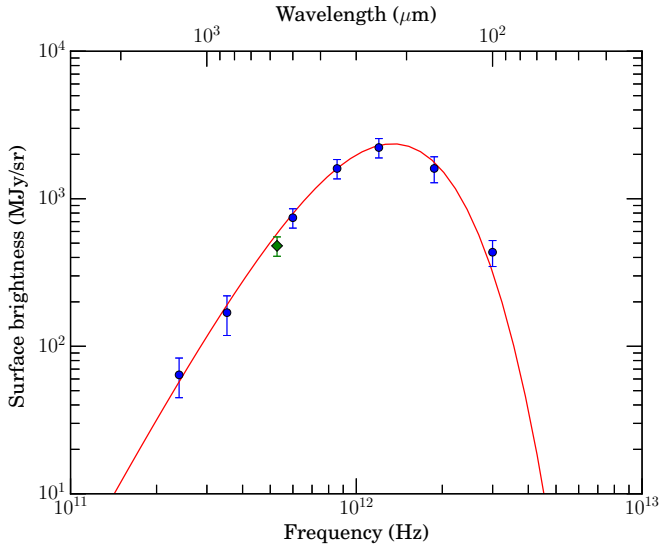


Fig. B.1: Spectral energy distribution of 16293E. The round blue dots are measurements from the continuum maps (PACS at $160\mu\text{m}$, SPIRE at 250, 350, and $500\mu\text{m}$, SCUBA-2 at $850\mu\text{m}$ and MPIfR bolometre at 1.3mm), the green diamond is the continuum measured on the ND spectrum. The red line is a modified blackbody law with a temperature of 14 K, an H_2 column density of $1.66 \cdot 10^{23} \text{cm}^{-2}$, and a dust emissivity spectral index β of 1.7.

absolute intensities were estimated to be 15% for PACS data, 20% for SPIRE data and 30% for ground-based data. With these values, we have tried to take into account the uncertainties due to large-scale diffuse emission components not related to the cloud, unknown thermal emission of the telescope, and filtering of the extended emission for the maps coming from ground-based telescopes, as well as the calibration errors quoted in Herschel's reports on extended emission calibration (Paladini et al. 2012;

Griffin et al. 2013). The continuum measured on the ND spectrum (which has a similar angular resolution of $41''$) is also plotted on the spectral energy distribution, and is consistent with the specific intensities measured from the continuum maps, within the uncertainties. In addition, we plotted a modified blackbody law accounting for the observed continuum emission at the various frequencies, following:

$$F_\nu = \kappa_0 \left(\frac{\nu}{\nu_0} \right)^\beta \mu m_{\text{H}} N_{\text{H}_2} B_\nu(T_{\text{d}})$$

where κ_0 is the dust emissivity coefficient at frequency ν_0 , μm_{H} the mean molecular mass, N_{H_2} the total H_2 column density and $B_\nu(T_{\text{d}})$ the black body thermal dust emission at temperature T_{d} . In Fig. B.1, we took $\kappa_0 = 0.005 \text{cm}^2 \text{g}^{-1}$ at $\nu_0 = 250 \text{GHz}$, $\beta = 1.7$, $\mu = 2.8$ (Kauffmann et al. 2008), $N_{\text{H}_2} = 1.66 \cdot 10^{23} \text{cm}^{-2}$ and $T_{\text{d}} = 14 \text{K}$. At the frequency of the NH observation, we estimate the continuum emission from the fit of the spectral energy distribution to be $\approx 2000 \text{MJy/sr}$, i.e. $\approx 0.07 \text{K}$ averaged over a beam of $\sim 36''$. For the purpose of comparison, for the same

beam size, the H₂ column density of the model discussed in Sec. 4 is $N_{\text{H}_2} = 1.5 \cdot 10^{23} \text{ cm}^{-2}$.